High-resolution reciprocal space mapping reveals dislocation structure evolution during 3D printing

Steve Gaudez, Kouider Abdellah Abdesselam, Hakim Gharbi, Zoltan Hegedüs, Ulrich Lienert, Wolfgang Pantleon, Manas Vijay Upadhyay

High-resolution reciprocal space mapping reveals dislocation structure evolution during 3D printing

S. Gaudez[1], K.A. Abdesselam[1], H. Gharbi[1], Z. Hegedues[2], U. Lienert[2], W. Pantleon[3], M.V. Upadhyay[1*]

[1] Laboratoire de Mécanique des Solides (LMS), CNRS UMR 7649, École Polytechnique, Institut Polytechnique de Paris, Palaiseau, France

[2] Deutsches Elektronensynchrotron (DESY), Hamburg, Germany

[3] Department of Civil and Mechanical Engineering, Technical University of Denmark (DTU), Kongens Lyngby, Denmark

[*] Corresponding author email: manas.upadhyay@polytechnique.edu

Keywords

Dislocations; Synchrotron diffraction; Solidification; Intrinsic heat treatment; Microstructure evolution

Abstract

Dislocation structures are ubiquitous in any 3D printed alloy and they play a primary role in determining the mechanical response of an alloy. While it is understood that these structures form due to rapid solidification during 3D printing, there is no consensus on whether they evolve due to the subsequent solid-state thermal cycling that occurs with further addition of layers. In order to design alloy microstructures with desired mechanical responses, it is crucial to first answer this outstanding question. To that end, a novel experiment has been conducted by employing high resolution reciprocal space mapping, a synchrotron-based X-ray diffraction technique, in situ during 3D printing of an austenitic stainless steel. It reveals that dislocation structures formed during rapid solidification undergo significant evolution during subsequent solid-state thermal cycling, in particular during addition of the first few (up to 5) layers above the layer of interest.

1 Introduction

3D printing has revolutionized the manufacturing sector through its unique ability to build near net shape parts without any tooling. 3D printing of alloys involves building parts in a layer-by-layer manner by melting a feed stock (powder or wire) using a moving heat-source (laser or electron beam). The ensuing heat and matter interaction subjects the material to a sequence of highly non-equilibrium processes until the end of building: melt-pool dynamics and rapid solidification is followed by heating-cooling cycles in the solid-state at varying temperature amplitudes and heating and cooling rates, also called solid-state thermal cycling (SSTC) or intrinsic heat treatment. These processes result in the formation of hierarchical microstructures exhibiting physical and chemical heterogeneity at multiple length scales [1–8].

Among the different possible microstructural features, dislocations are ubiquitous in any as-built alloy. They mainly organize in intragranular cell structures with a high dislocation density in the cell walls and a low density in the cell interiors. These dislocation cells are among the smallest heterogeneities in as-built alloys and play a primary role in enhancing the yield strength of the material often accompanied by a lower ductility [4–6]. Designing alloy microstructures that exhibit desired material properties necessitates control of the 3D printing process parameters to obtain appropriate dislocation structures. Achieving such control first requires a thorough understanding of the role of different non-equilibrium processes occurring during 3D printing on the formation of the dislocation structures and their evolution into their final form in an as-built alloy.

Currently, there are two main hypotheses on the origin of dislocation cells in as-built alloys. One hypothesis is that these cells form in inter-dendritic regions during rapid solidification and do not significantly evolve, if at all, during SSTC. This hypothesis is based on post-build electron microscopy observations of dislocation cells coinciding with microsegregations in inter-dendritic regions [5,9]; the latter are a signature of directional solidification in 3D printed alloys. The opposing hypothesis is that the thermo-mechanical forces occurring during SSTC result in significant changes in the dislocation structures formed during rapid solidification. This hypothesis is motivated from other post-build electron

microscopy studies [10–14] presenting observations that dislocation cells do not always coincide with microsegregations. How ever, both the aforementioned hypotheses are based on studies performed after samples have been printed; yet, it is impossible to univocally separate the role of SSTC from that of solidification on dislocation structure and internal stress formation and evolution during 3D printing by solely analyzing as-built samples. A clear insight into the effects of the different processes can only be gained by tracking the evolution of dislocation structure and internal strains in situ during 3D printing.

To that end, we conducted a novel experiment involving high-resolution reciprocal space mapping (HRRSM), a synchrotron-based X-ray diffraction technique, while 3D printing samples from an austenitic stainless steel. HRRSM involves using a narrow beam (slightly larger than the grain size) of high-energy monochromatic X-rays to record a diffraction pattern from a single grain embedded in the bulk material, and generating a 3D reciprocal space map of the crystal lattice of that grain [15–19]. From these maps, the intragranular distributions of lattice strain and orientation can be extracted. Performing HRRSM of selected grains at different intervals during 3D printing allows tracking the evolution of their intragranular distributions of lattice strain and orientation. In the case of an austenitic stainless steel, major intragranular variations are related to dislocation evolution (with a potential minor contribution of heterogeneous grain environments); there are no contributions from solid-state phase transformations. This experiment provides, for the first time, an unambiguous answer on the importance of SSTC during 3D printing in evolving the dislocation structures and intragranular strains obtained after solidification.

2 Materials and methods

The experiments were conducted using a newly designed miniature laser metal deposition (mini-LMD) machine (Fig. 1.a) dedicated to per forming in situ and operando synchrotron X-ray experiments; a detailed description of the machine is provided in Appendix A. 3D printing was performed using a single-phase 316L austenitic stainless steel (316LSS). The 316LSS powder feedstock had been prepared via inert gas atomization by Oerlikon AM (Germany) and has a chemical composition (in wt%) of Fe–17.34Cr–12.55Ni–2.34Mo–1.4Mn–0.49Si–0.08N–0.04Cu–0.03O (with trace elements P (0.01 wt%), Si (less than 0.01 wt%), and C (less than 0.01 wt%)). The powder particle size distribution had a median of 58 µm, and the 10% and 90% quantiles were ∼44 µm and ∼82 µm, respectively. The following 3D printing parameters and strategy were used to build thin-wall type samples were used: single track per layer unidirectional printing, laser power 100 W, printing speed 600 mm/min, powder flow rate 7 g/min, and vertical displacement of focusing head 0.25 mm between each layer. Each thin wall was printed on a hot-rolled, annealed, pickled, and sanded 316LSS plate of $40(x) \times 140(y) \times 10(z)$ mm^3 with the following composition (in wtFe–16.52Cr–10.08Ni–2.08Mo–1.31Mn–0.5Si–0.36Cu–0.31Co–0.024C.

The mini-LMD machine was installed at the P21.2 beamline of the PETRA III synchrotron of Deutches Elektronen-Synchrotron (DESY, Germany) where HRRSM can be performed in transmission mode. A 2D detector was positioned in the horizontal diffraction plane (Fig. 1.b) to acquire diffraction patterns of 400 (γ-austenite) diffraction peaks. Therefore, all investigated grains had one of their <100> directions close to the printing direction. HRSSM was performed using a 52.5 keV X-ray beam of size 300×300 µm^2 and having a narrow bandwidth (0.009 keV) and negligible divergence. The detector records diffraction patterns along two of the three directions in reciprocal space: the radial direction corresponding to the diffraction angle 2θ, which is related to the interplanar spacing d_{hkl} through Bragg's law, and one azimuthal direction corresponding to the angle η around the $+x$ axis. To obtain information along the other azimuthal direction corresponding to the angle ω (Fig. 1.b), and thus 3D reciprocal space maps of 400 diffraction peaks, the specimen is rocked around the $+z$ axis ($\omega = \pm 2°$ and detector images are acquired in intervals of 0.02°). A detailed description of the experimental setup and data acquisition is given in Appendix B. Acquired detector images from each grain were treated using the procedure described in Appendix B, and illustrated in Fig. 1.b, to obtain the 3D reciprocal space map of that grain. Angular resolution of $\Delta 2\theta = 0.0026°$, $\Delta\eta = 0.0025°$, and $\Delta\omega = 0.02°$ was reached with the current setup.

Grains that can be considered suitable for HRRSM investigations have to fulfill the following criteria: (i) they must have one of their <100> crystallographic directions nearly parallel to the printing direction ($-y$), (ii) they must be completely illuminated by the beam, and (iii) their 400 diffraction peaks must be well separated in azimuthal directions (i.e., angles η and ω) from the 400 diffraction peaks of other grains illuminated simultaneously by the beam.

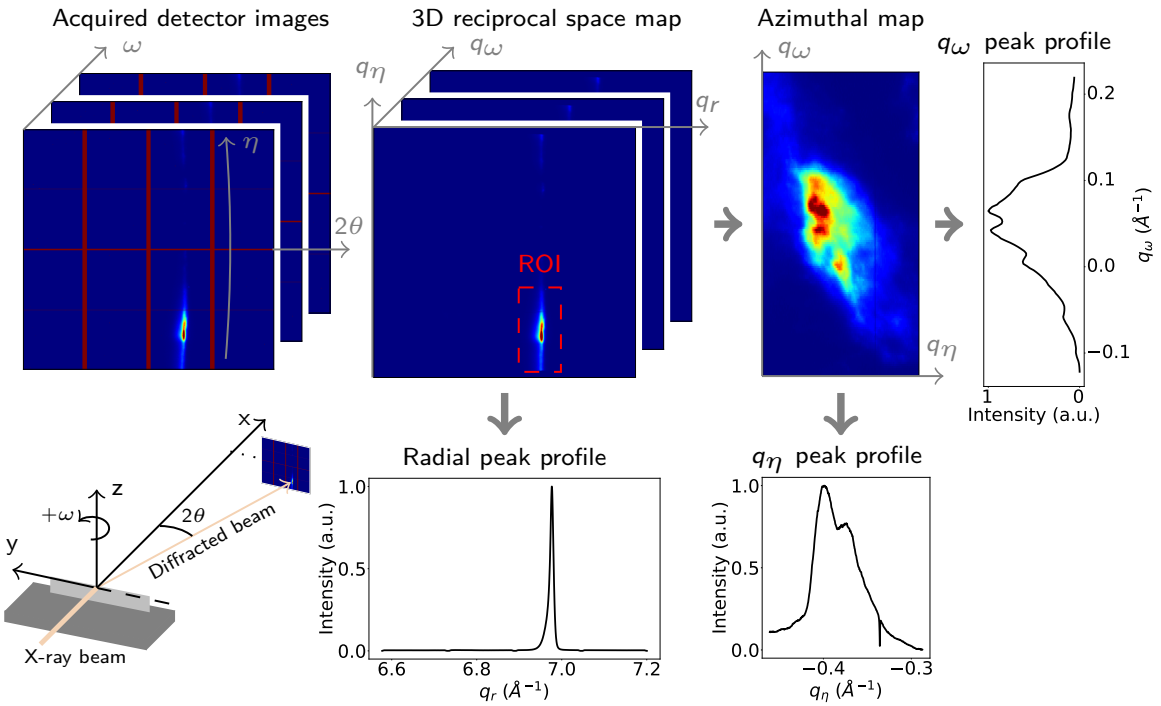

Figure 1: Experimental setup and procedure: (a) The mini-LMD machine: A perspective view of the machine showing a wall sample being built as well as the direction of the incoming and diffracted X-ray beam. (b) HRRSM data acquisition and treatment for a grain: During mapping of each grain, the sample was rocked continuously about the vertical z axis. The acquired raw data are treated to obtain a 3D (q_r, q_η, q_ω) reciprocal space map of a 400 diffraction peak of a grain having one of its <100> directions close to the printing direction (Eq. 1). Projection from the region of interest (ROI) of this map onto the azimuthal plane (q_η, q_ω) reveals the intragranular orientation distribution, and projection along the radial direction (q_r) provides the radial peak profiles. Azimuthal maps can also be projected along q_η and q_ω to obtain azimuthal peak profiles. (c) An illustration depicting each step of the experimental procedure.

The experimental procedure (illustrated in Fig. 1.c) to print the two thin-wall samples was: (i) Print $L_0 = 20$ layers using a single-pass-per-layer unidirectional printing strategy and let the sample cool down to room temperature. (ii) Using the X-ray beam, identify multiple grains of interest (those having one of their <100> crystallographic directions along the printing direction, $-y$ in Fig. 1) in the topmost layer (L_0) within a region close to the center of the sample and perform HRRSM for each grain. At this stage, these grains have only experienced rapid solidification and cooling down to room temperature; hence, their 3D reciprocal space maps are taken as reference for the as-solidified state. (iii) Add a set of n layers on top of the sample using the same printing strategy. (iv) Re-perform HRRSM on each of the previously identified grains. (v) Repeat the previous two steps until the end of building.

Two thin-walls were printed (along y) 5 mm away (along x) from the substrate edge that is closest to the Kapton window for the outgoing X-ray beam and they were centered along y on the substrate. One of the two samples, denoted as S5L, was built in intervals of $n = 5$ layers to a total of 80 layers i.e., L_0 + 60 layers. The other sample, denoted as S2L, was built in intervals of $n = 2$ layers to a total of 40 layers i.e., L_0 + 20.

3 Results

An inert gas atomized 316LSS powder was used to build two thin-wall samples on two 316LSS substrates *in situ* at the P21.2 beamline of PETRA III synchrotron (DESY, Germany) using the aforementioned procedure (Section 2). Three grains were identified in the L_0 (20th) layer for S5L and were named

S5L-G1, S5L-G2 and S5L-G3. Two grains were identified in the L_0 (20th) layer of S2L and were named S2L-G1 and S2L-G2. All grains were in the size range [38,110] µm and smaller than the beam size; therefore, in each case the entire grain is illuminated. From each 3D reciprocal space map, projections were derived along the radial direction (q_r) and in the azimuthal plane (q_η, q_ω) as seen in Fig. 1.b. The evolution of these projections was followed as a function of added layers.

3.1 Radial peak profiles

The radial peak profiles $I_n(q_r)$ computed using Eq. 2 are asymmetric for all grains with a pronounced tail towards lower q_r; an example is shown for S5L-G1 in Fig. 2.a. This asymmetry is mainly caused by the presence of Cr-Mo microsegregation structures; see Appendix B.3. These microsegregation structures are formed during solidification and do not evolve significantly during SSTC [20], which is substantiated by negligible changes in peak asymmetry after layer addition (Fig. 2.a).

However, adding layers changes the average peak position and the integral width. For all grains, the average peak position first shifts towards lower q_r after addition of the first set of layers and then with further addition of layers moves gradually towards higher q_r. These back-and-forth shifts, shown for S5L-G1 in Fig. 2.a, are caused by the evolution of intergranular residual lattice strains. They can be better understood by studying the evolution of the average lattice strain (along y in Fig.1), derived from average peak positions using Eq. 5, as a function of added layers for all grains as shown in Fig. 2.b. In the as-solidified state, all grains have a residual tensile strain of ∼0.22% with respect to the strain-free lattice spacing (see Appendix B). These tensile strains are a consequence of the temperature gradient mechanism [21] occurring during local cooling of a single-phase material. After addition of a few layers, the residual tensile strain of each grain increases and reaches a maximum; in the present case, the maximum occurs after adding either five layers to L_0 (i.e., $L_0 + 5$) or four layers to L_0 (i.e., $L_0 + 4$) respectively for the S5L and S2L strategies. With further addition of layers, a continuous decrease in the residual lattice strain of each grain is observed. The final residual lattice strains for all grains are lower than the ones at L_0 but they remain tensile. These results show that the maximum grain-averaged tensile strain occurs a few layers below the topmost layer i.e., in layers which have experienced some SSTC. Since all the HRRSM measurements are performed at room temperature, the observed changes in lattice strains can only be caused by the presence of other phases (e.g., ferrite) or mechanical constraints imposed by the substrate on the printed walls. A quantitative phase analysis using Rietveld refinement [22] was performed on diffraction patterns acquired from the as-built samples using another 2D detector much closer to the sample. It revealed that the samples were dominantly austenite with only a trace amount of ferrite (less than 0.25%). The observed changes in lattice strains cannot be explained by such a small amount of a second phase, but must be caused by the macroscopic mechanical constraints.

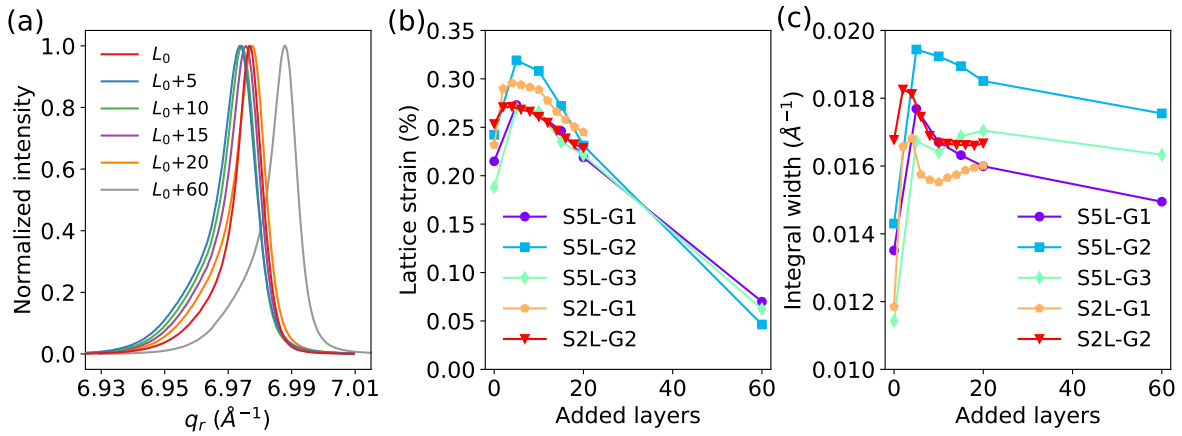

Figure 2: Evolution along the radial direction: (a) Radial peak profiles of S5L-G1 with respect to the number of added layers. The intensity of the radial peak profile is normalized using Eq. 2. Evolution of (b) residual lattice strain and (c) integral width, obtained from the radial peak profiles, as a function of the number of added layers for all five grains from S5L and S2L.

The integral widths, calculated using Eq. 6, of all grains also increase after adding the first few layers (5 layers for S5L and 2 or 4 layers for S2L) as seen in Fig. 2.c. Further addition of layers yields three different behaviors: (i) a continuous decrease until the end of building for S5L-G1 and S5L-G2, (ii) an initial decrease followed by a constant integral width for S2L-G2, and (iii) a decrease followed by a slight reincrease for S5L-G3 and S2L-G1.

These integral widths are composed of convoluted contributions from instrumental broadening, size broadening and intragranular lattice strain distribution; dislocation cells can play a significant role for the latter two contributions. However, these contributions cannot be separated using standard methods, such as the modified Williamson-Hall approach [23], because they require information from more than one radial peak profile. Furthermore, it is also not possible to perform a single peak profile analysis [24] due to the asymmetry caused mainly by microsegregations.

3.2 Aimuthal maps

To univocally prove that dislocation evolution indeed occurs due to SSTC during layer addition, azimuthal maps containing information on intragranular orientation distribution are studied. Fig. 3 shows the azimuthal maps of all the investigated grains acquired at room temperature in the as-solidified state and after several subsequently added layers. Each map shows either a single maximum or multiple local maxima occurring on a cloud of lower intensity. Several effects may contribute to these azimuthal distributions: (i) a homogeneous bending and twisting of the investigated grain due to type II stresses [25] from its neighborhood resulting in a constant intensity within the clouds. (ii) Local bending and twisting induced by randomly distributed dislocations or thick dislocation walls resulting in smooth intensity variation within the clouds. (iii) Localized finite orientation differences induced by dislocation boundaries resulting in intragranular orientation domains (ODs) [16,19]. Such ODs manifest themselves in azimuthal maps as distinguishable regions of enhanced intensity around local intensity maxima separated from other ODs by regions of lower intensity.

In the as-solidified state (L_0 in Fig. 3), multiple regions of enhanced intensity with distinct maxima can be identified in the azimuthal maps of S5L-G1 and S5L-G3. They indicate the existence of individual ODs with slightly different orientations between them caused by the presence of dislocation boundaries. Meanwhile, clouds with smoothly varying intensity and a single maximum can be identified in the azimuthal maps of the remaining grains indicating a more homogeneous dislocation distribution.

After addition of the first set of layers ($L_0 + 5$ or $L_0 + 2$), the $I_n(q_\eta, q_\omega)$ intensity distributions have broadened and the azimuthal maps of all grains have significantly changed. For S5L-G1, the distinct ODs with multiple local maxima are replaced by a single OD with large spread and one maximum. S5L-G2 and S2L-G2 have developed a larger spread with multiple local maxima. Meanwhile, S5L-G3 and S2L-G1 have developed distinct ODs with their own spread and local maxima. Recalling that microsegregations do not evolve significantly during layer addition, it can be concluded that the changes in the azimuthal maps are due to dislocation structure evolution.

Furthermore, average peak positions in q_η and q_ω have changed significantly for all grains. They reflect rotations of entire grains in η and ω and can be quantified by the peak shifts Δq_η and Δq_ω shown in Fig. 4.a and b, respectively. Significant overall grain rotations are observed after the addition of the first set of layers. The grains mainly rotate anti-clockwise in η and clockwise in ω (cf. coordinate system in Fig. 1), except for one grain in each case. The magnitude of rotation is different for each grain, with large changes (e.g., S5L-G3) and small changes (e.g., S2L-G1) along both q_η and q_ω. Besides intragranular dislocation evolution, heterogeneous deformation of the grain neighborhood may also contribute to these rotations.

The developing spread in azimuthal maps can be quantified by the standard deviations in q_η and q_ω, which reflect the changes in widths of the projected $I_n(q_\eta$ and $I_n(q_\omega$ profiles; their changes are shown in Fig. 4.c and d, respectively. All grains exhibit a strong increase in their azimuthal spread after the addition of the first set of layers but subsequent addition of layers has only a minor effect. From these results, it can be concluded that dislocation structures significantly evolve during the addition of a first few layers (i.e., during the initial stages of SSTC), specifically up to 5 layers, while no significant evolution occurs later even though the lattice strains continue to evolve.

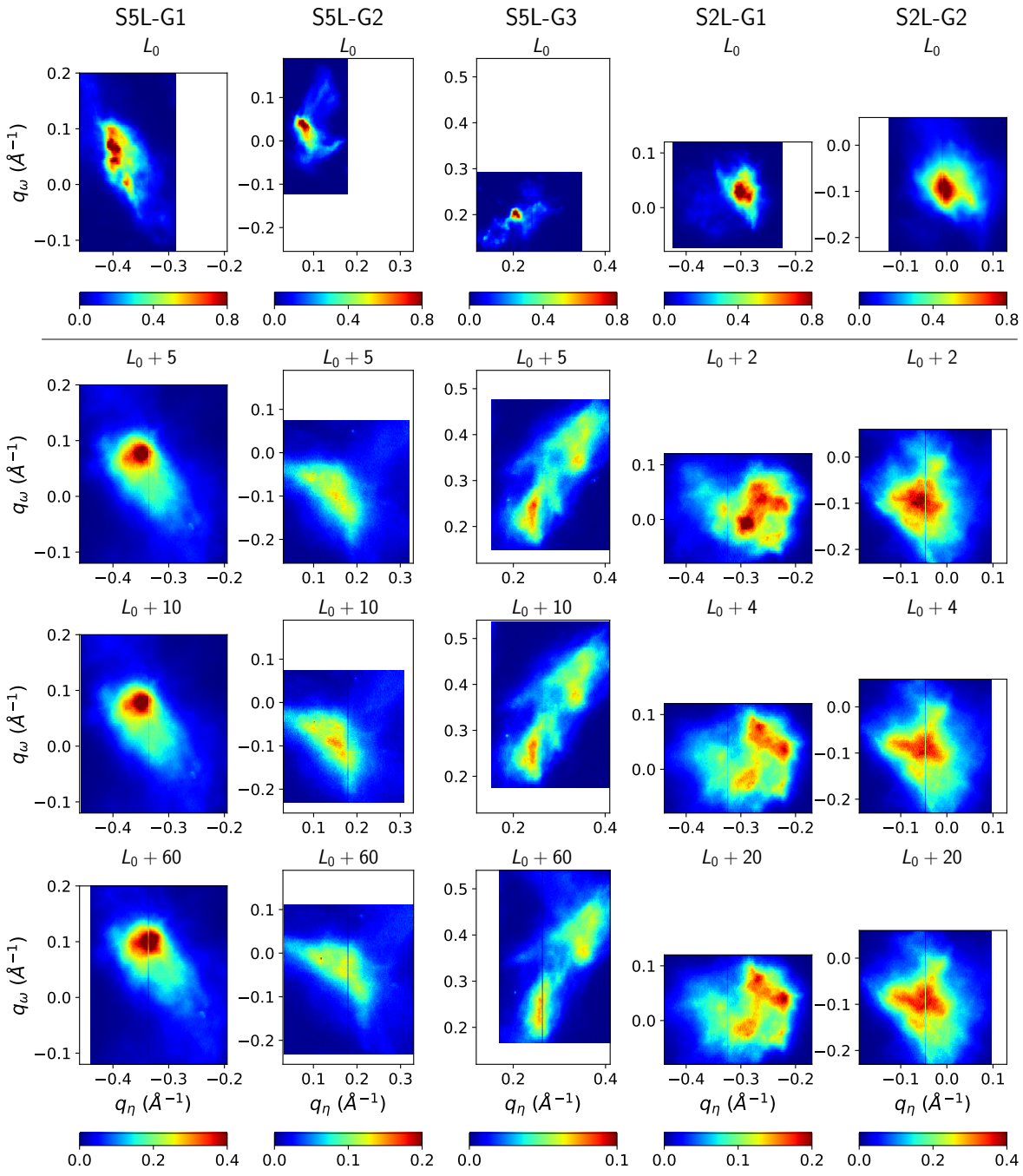

Figure 3: Azimuthal maps of the five investigated grains in their initial as-solidified state when L_0 is the topmost layer, and after addition of the first $(L_0 + n)$, the second $(L_0 + 2n)$, and the last $(L_0 + N)$ set of layers; here $n = 5$ or 2 and $N = 60$ or 20 for S5L or S2L, respectively. The intensity within each azimuthal map is normalized using Eqs. (B.3) and (B.4). Low intensity vertical lines are caused by interpolation over inactive areas on the detector.

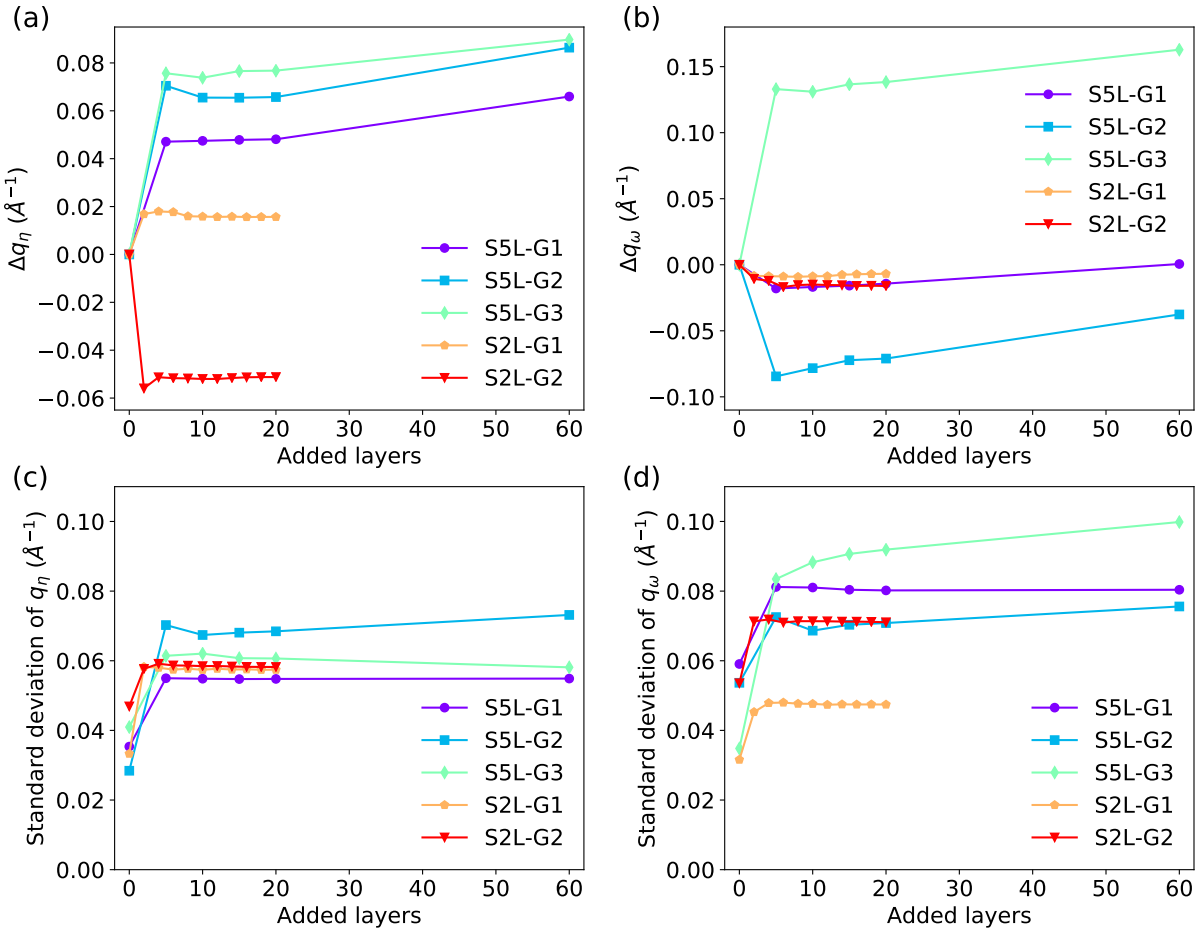

Figure 4: Evolution of peak shift and standard deviation of azimuthal peak profiles: Evolution of the shift in the average peak positions of the azimuthal peaks along (a) $q_\eta(\Delta q_\eta)$ and (b) $q_\omega(\Delta q_\omega)$ and the standard deviations of (c) q_η and (d) q_ω as a function of the number of added layers for all grains.

3.3 Intragranular orientation domains

To investigate the microstructure evolution within grains, individual ODs within a grain were precisely identified following the procedure in [16,19] and their evolution tracked during 3D printing. The analysis is restricted to S5L-G3 and S2L-G1 because ODs in these grains were clearly distinguishable not only after the first set of added layers ($L_0 + 5$ and $L_0 + 2$, respectively) but also until the end of building.

ODs were identified based on the azimuthal maps obtained after the first set of layers had been added. Each OD is defined through a region of interest in the azimuthal map containing one or more local intensity maxima in such a way that there is no overlap with the region of interest of other ODs. Note that dislocation structures resolved on the level of these ODs do not correspond to individual dislocation cells. The latter could not be identified because it is impossible to separate high intensity peaks associated with individual cells within these ODs, mainly due to the finite size broadening from the small coherently scattering size of individual cells.

For both S5L-G3 and S2L-G1, two ODs are defined as shown in Fig. 5.a and d. The evolution of their lattice strains (Fig. 5.b and e) and integral widths (Fig. 5.c and f) are followed as a function of added layers and compared to the average evolutions of the entire grains presented in Fig. 2.b and c. The size of the regions of interest were kept constant during the analysis, but their positions were slightly adjusted to allow following the rotations of the ODs with layer additions.

The lattice strains in OD1 and OD2 of both grains evolve similar to that of their respective grain, but with a positive and negative offset, respectively, i.e., OD1 and OD2 experience higher and lower tensile strains than the grain average. These lattice strain differences between ODs (up to 0.027%) contribute to the integral width of the entire grain.

The integral width of OD1 of S5L-G3 initially evolves in a manner similar to that of the entire grain. It decreases between addition of 5 and 10 layers, re-increases while adding 10 more layers, and then increases slightly towards the end of printing. Meanwhile, the integral width of OD2 starts much lower than that of the entire grain and OD1, and becomes even lower with further addition of layers. For grain S2L-G1, the integral width evolves in a strikingly different manner. It initially increases for the grain and both its ODs until the addition of four layers. During addition of six more layers, all integral widths decrease. Afterwards, until the end of the process, they re-increase for the entire grain and OD1, but decrease for OD2. At the end of building, the integral widths of both ODs are nearly the same.

Focusing on S2L-G1, it becomes clear that lattice strains and integral widths increase for both of its ODs during the addition of the first four layers. Hence, the increase in integral width of the entire grain cannot be attributed to the development of different tensile strains in both ODs, but rather to the accumulation of dislocations due to plastic deformation after the first sets of added layers. Adding more than four layers leads to a reduction in integral width of each OD and the entire grain; it must also be a consequence of dislocation rearrangement (or annihilation) during SSTC leading to mutual screening of the elastic strain fields from dislocations.

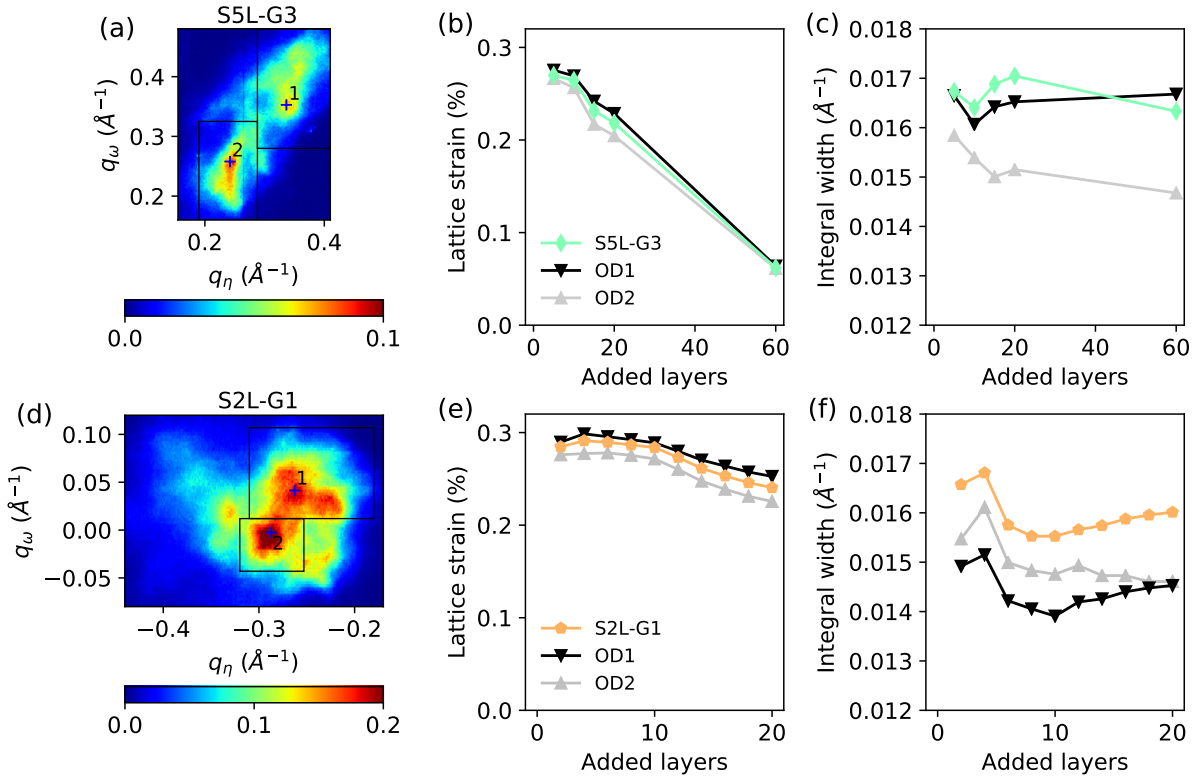

Figure 5: Investigating orientation domains (ODs) within two selected grains (a-c) S5L-G3 and (d-f) S2L-G1: The rectangles shown in the azimuthal maps after the first set of layers added (a: $L_0 + 5$, d: $L_0 + 2$) indicate regions of interest defining two ODs in each grain. The plus signs indicate the position of the maximum intensity in each OD. Evolution of (b, e) lattice strain and (c, f) integral width of the entire grain (S5L-G3 or S2L-G1) and their respective ODs as a function of the number of added layers.

4 Discussion and conclusions

A plethora of notable changes were observed in the diffraction patterns of investigated grains in the L_0 layer due to SSTC induced by the addition of layers above L0, in comparison to their as-solidified state (when L0 was the topmost layer). The radial peak profiles (Fig. 2) and the azimuthal maps (Fig. 3) revealed an evolution of the intragranular structure and the development of residual strains in individual grains with the addition of layers. Peak shifts in the radial direction are mainly governed by developing type II residual stresses of each grain. Meanwhile, the increasing integral width in radial as well as

azimuthal directions respectively reveals the formation of intragranular (type III) residual stresses and orientation differences within grains. Development of local differences in strain and orientation within a grain can be either imposed by the neighborhood of the investigated grain or a consequence of heterogeneous plastic deformation of the grain. The large increase in integral width and azimuthal spread after the addition of the first set of five layers for S5L indicates that changes to the dislocation structure due to plastic deformation must occur during SSTC. For printing strategy S2L, the largest increase is observed after adding the first two layers. However, a continued increase in azimuthal spread and integral width is observed for grain S2L-G1 with the addition of two more layers. The most plausible explanation, which is that dislocation structures evolve during SSTC, is further substantiated by the azimuthal maps developing distinct ODs (Fig. 5). The development of such large orientation spreads and finite misorientations between ODs cannot occur purely from elastic bending (or twisting) induced by surrounding grains; the latter would induce continuous curvatures leading to smooth intensity distributions instead of the observed distinct ODs.

Considering the collected evidence from 3D reciprocal space maps, it becomes apparent that the dislocation structures that manifest just after solidification evolve significantly during the initial stages of SSTC i.e., after adding a few layers on top of the investigated region. In other words, the dislocation structures obtained at the end of a 3D printing process are not the same as those obtained just after solidification.

Recently, a dislocation thermo-mechanics model [26] had been developed with the aim to predict dislocation evolution during transient and heterogeneous temperature changes such as those occurring due to SSTC during 3D printing. Our findings validate the core assumption of this model, which is that dislocations can evolve during SSTC. Our experiment also paves the way to better understand the thermo-mechanics of dislocations during 3D printing and to perform more dedicated simulations e.g., as done in [27] using a discrete dislocation dynamics approach. Such simulations would allow tailoring the dislocation structures in 3D printed parts by subjecting them to in-process heat treatments, e.g., using one or more lasers to change the dislocation structure locally and globally. Since dislocation structures play a primary role in determining the mechanical properties of a material, such in-process heat treatments could be used to tune the eventual mechanical response of a part.

Funding

This work was supported by the Horizon 2020 - EXCELLENT SCIENCE - European Research Council Starting Grant 2020 project GAMMA (Grant agreement ID: 946959) awarded to MVU.

CRediT authorship contribution statement

Upadhyay Manas Vijay: Writing – review & editing, Writing – original draft, Supervision, Resources, Project administration, Methodology, Investigation, Funding acquisition, Formal analysis, Conceptualization, Validation. Pantleon Wolfgang: Writing – review & editing, Writing – original draft, Visualization, Supervision, Methodology, Investigation, Conceptualization, Formal analysis. Lienert Ulrich: Writing – review & editing, Methodology, Investigation, Conceptualization. Hegedüs Zoltan: Writing – review & editing, Methodology, Investigation. Gharbi Hakim: Writing – review & editing, Methodology, Investigation. Abdesselam Kouider Abdellah: Writing – review & editing, Methodology, Investigation. Gaudez Steve: Writing – review & editing, Writing – original draft, Visualization, Methodology,Investigation, Formal analysis.

Declaration of competing interest

The authors declare that they have no known competing financial interests or personal relationships that could have appeared to influence the work reported in this paper.

Data availability

Data will be made available on request.

Acknowledgments

We acknowledge the support of DESY (Hamburg, Germany), a member of the Helmholtz Association HGF, for the provision of the synchrotron facility. SG, KAA, HG and MVU are grateful to the European Research Council (ERC) for their support through the European Union's Horizon 2020 research and innovation programme for project GAMMA (Grant agreement No. 946959) awarded to MVU. The

experiments were carried out at the P21.2 beamline of the PETRA III synchrotron. Beamtime was allocated for proposal no. I-20210525 EC. WP acknowledges support from the EuroTech Visting Researcher Program and thanks the Danish Agency for Science, Technology, and Innovation for funding the instrument center DanScatt.

A Mini-LMD machine

In situ and *operando* synchrotron X-ray techniques are powerful tools used to investigate and understand the mechanisms occurring during the 3D printing processes (e.g., melt pool dynamics, defects formation, and solid-state phase transformation). Several machines dedicated to synchrotron experiments have been developed and used to study a broad range of 3D printing techniques and materials, e.g., [28,29]. However, most of the machines allow printing relatively small sized parts with simple printing strategies.

A newly designed miniature laser metal deposition (mini-LMD) machine dedicated to performing *in situ* and *operando* synchrotron and neutron experiments has been developed to overcome these constrains. The machine was designed to print large scale parts (semi-industrial), using a broad range of printing strategies (e.g., unidirectional, bidirectional, cross-hatch, etc.), and under inert environment for oxygen reactive metals such as Ti and Al based alloys. The mini-LMD machine has been designed in collaboration with Sotimeco company (France). Fig. 6 shows (a) the design of the machine and its main components and (b and c) pictures of the machine installed at the P21.2 beamline (DESY PETRA III, Germany).

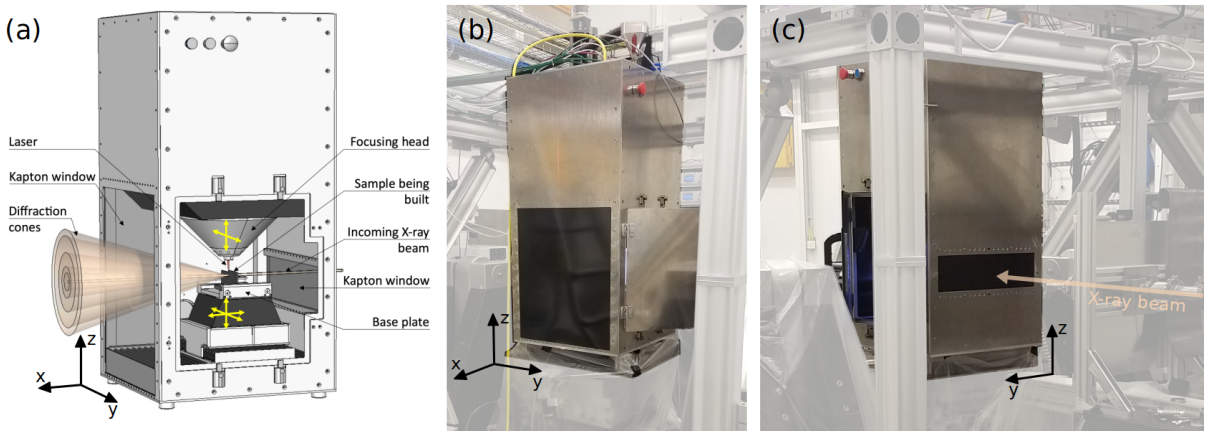

Figure 6: (a) A perspective view of the machine showing a wall sample being built as well as the direction of the incoming and diffracted X-ray beam and (b and c) pictures of the mini-LMD machine installed at the P21.2 beamline.

The mini-LMD machine is $500(x) \times 500(y) \times 1100(z)$ mm^3 in size and it weighs about 100 kg. Its walls are made from an aluminum alloy. The front and back walls (perpendicular to x) of the printing chamber are equipped with two Kapton polyimide (grade Cirlex CL) windows of 0.76 ($\pm$10%) mm thickness; these windows are opaque to the emitted laser radiation but transparent to X-rays. The machine is hermetically sealed, preventing laser radiation or powder particles from leaking outside. The front Kapton window of size $430(y) \times 200(z)$ mm^2 is situated on the X-ray entrance side and the back one of size $430(y) \times 430(z)$ mm^2 is situated on the X-ray exit side (Fig. 6). The sample positioning and the size of the Kapton windows are such that full Debye-Scherrer rings with diffraction angles up to 30° can be recorded. The printing chamber inside the machine can be accessed through a door locked by a magnetic interlock security system. This chamber is equipped with a focusing head having two translation stages: x and y, and a base plate having three translation stages: x, y, and z. The translation stages have a maximum travel speed of 33 mm/s. The base plate is water-cooled at 25 °C via a water-based chiller (PRC Laser). The mini-LMD can manufacture parts of sizes up to $100(x) \times 100(y) \times 80(z)$ mm^3 using either the focusing head or the base plate.

The mini-LMD is equipped with a high-energy continuous-wave fiber laser (PRC Laser) of wavelength 1080$\pm$1 nm with a maximum power of 1000 W. The laser spot size at the focusing distance is

approximately 0.4 mm. The laser beam is tilted by 20° with respect to the vertical axis of the focusing head and can rotate over 360° around it, which adds an additional degree of freedom for printing along with the focusing head and base plate motions. The powder is stored in a funnel-like tank inside the machine which moves with the focusing head. The humidity inside the tank is controlled by an external drying (W-Tech) system coupled with a pump. An endless screw and argon gas are used to transport the powder from the tank to a 1 mm diameter tungsten carbide nozzle aligned with the vertical axis of the focusing head. To minimize oxidation of the melt pool during manufacturing, argon is also used as a shielding gas. In addition, the printing chamber can be flushed with inert gas allowing the printing of high oxygen reactive alloys. The oxygen level inside the chamber is monitored via an oxygen transmitter 600 mk3 (Systech Instruments). The machine includes a powder iltration system (TBH GmbH) with a high-efficiency particulate air 13 HEPA filter (H13 HEPA filter) that automatically vacuum suspended powder particles at the end of the printing process. Every piece of equipment is connected to an elctrical cabinet and managed by one computer and one control panel that can both be used and controlled outside of the experimental hutch.

B HRRSM

B.1 Setup and acquisition

The mini-LMD machine was installed at the P21.2 beamline of the PETRA III synchrotron of DESY (Germany), where HRRSM can be performed in transmission mode. An Eiger CdTe 4M (Dectris) detector was used to acquire two-dimensional diffraction patterns of 400 (γ-austenite) peaks of 316LSS. This detector has an active area of 2162 × 2068 pixels (along y and z as defined in Fig. 1) with a pixel size of 75 × 75 µm^2. Using Bragg's law ($2d_{hkl}\sin(\theta) = \lambda$, where d_{hkl} is the interplanar spacing between the diffracting hkl lattice planes and $\lambda = 0.23616$ Åis the X-ray wavelength corresponding to 52.5 keV X-ray energy) and the strain-free lattice constant $a_0 = 3.59346$ Å, the diffraction angle $2\theta \approx 15.05°$ is obtained for the 400 reflection. To perform HRRSM, the detector was positioned at 6.48 m (along the beam direction x) downstream of the sample and at ∼1.75 m from the incident beam direction (along the printing direction, $-y$, as shown in Fig. 1.b), which allowed capturing the intensity distributions of 400 (γ-austenite) diffraction peaks of 316LSS that are close to the horizontal diffraction plane. All investigated grains had one of their <100> directions close to the printing direction.

The detector records diffraction patterns along two of the three directions in reciprocal space: the radial direction corresponding to the diffraction angle 2θ, which is related to d_{hkl} through Bragg's law and one azimuthal direction corresponding to the angle η around the $+x$ axis. To obtain information along the other azimuthal direction corresponding to the angle ω (Fig. 1), the specimen is rocked around the $+z$ axis. In order to perform such rotations, the mini-LMD machine is placed on a diffractometer available at the beamline, which allows rotations around different axes. During acquisition of 3D reciprocal space maps, the mini-LMD is continuously rotated with constant speed around the $+z$ axis while collecting diffraction patterns in the range $\omega = [-2°, 2°]$; the maximum and minimum values are adapted to the azimuthal spread of the diffraction peak investigated, however, the spread of the intensity distribution never exceeded 4°. Synchronization of rotation and detector acquisitions ensures that each image represents a small angular interval $\Delta\omega = 0.02°$ and an acquisition time of 1 s. Both azimuthal angles η and ω are defined to increase anti-clockwise around their respective axes (Fig. 1).

With this experimental setup, a high angular resolution of $\Delta 2\theta = 0.0026°$ is obtained along the radial direction for the 400 diffraction peak and it is dominated by the energy band width with negligible contributions from beam divergence, pixel size on the detector and size of the investigated grains. The resolution $\Delta\eta = 0.0025°$ along η is dominated by the pixel size with additional contributions from the beam divergence and the size of the investigated grains. The angular resolution along ω is mainly determined by the chosen rocking interval $\Delta\omega$, which is 0.02°.

B.2 Data treatment

Each acquired image was binned (into 2162 and 2068 bins) to obtain an azimuthal angle versus scattering angle (η vs 2θ) map using the pyFAI python library [30]; the number of bins in both directions were defined by the pixel array format of the images. The angles from the acquired (2θ, η, ω) maps for each

grain were transformed into reciprocal space coordinates using the following formulae [19]:

$$\begin{aligned} q_r &= \frac{4\pi}{\lambda}\sin(\theta) \\ q_\eta &= \frac{2\pi\eta}{\lambda}\sin(2\theta) \\ q_\omega &= \frac{4\pi\omega}{\lambda}\sin(\theta) \end{aligned} \tag{1}$$

For each grain, a 3D reciprocal space map is then obtained by stacking the images where two dimensions (q_r and q_η) are covered by the detector and the third dimension q_ω is obtained from the rocking angle ω. In order to keep only the information relevant for the chosen diffraction peak, a region of interest in (q_r, q_η, q_ω) is defined for each 3D reciprocal space map in such a way that it covers the entire diffraction peak. The binned 3D reciprocal space map is then projected to obtain the two different projections shown in Fig. 1.b: the radial peak profile $I(q_r)$ by integrating over q_η and q_ω and the azimuthal map $I(q_\eta, q_\omega)$ by integrating over the radial direction along q_r. The radial peak profile is normalized according to:

$$I_n(q_r) = [I(q_r) - \min I(q_r)]/[\max I(q_r) - \min I(q_r)] \tag{2}$$

The intensity distributions in all azimuthal maps are initially normalized with respect to the average intensity in the map:

$$I'(q_\eta, q_\omega) = I(q_\eta, q_\omega)/\left(\int I(q_\eta, q_\omega)dq_\eta dq_\omega / area\ of\ azimuthal\ map\right) \tag{3}$$

Finally, for each grain, the intensities in the azimuthal maps are reported relative to the intensities of the initial azimuthal map of the grain at layer L_0 as:

$$I_n(q_\eta, q_\omega) = [I'(q_\eta, q_\omega) - \min I'_{L_0}(q_\eta, q_\omega)]/[\max I'_{L_0}(q_\eta, q_\omega) - \min I'_{L_0}(q_\eta, q_\omega)] \tag{4}$$

The radial peak profiles, which are asymmetric with a long tail along the low diffraction vectors as seen in Fig.2.a, are fitted with a constant background and a superposition of two Pearson VII functions. The average radial peak position of the entire peak is determined as the integrated intensity weighted average position of the two Pearson VII functions.

The residual elastic strains, averaged over a grain, are determined from the average position $2\theta_{hkl}$ along the radial profile of an hkl peak from the corresponding interplanar spacing d_hkl between hkl planes:

$$\varepsilon_{hkl} = \ln(d_{hkl}/d_{hkl,0}) = \ln(\sin\theta_{hkl,0}/\sin\theta_{hkl}) \tag{5}$$

where ε_{hkl} is the true elastic strain, $\theta_{hkl,0}$ (half of) the strain free diffraction angle, θ_{hkl} (half of) the measured diffraction angle, and $d_{hkl,0}$ is the strain-free interplanar spacing.

The strain-free lattice parameter a_0 used to determine $d_{hkl,0}$ is obtained from the feedstock powder. This approach has several advantages: (i) the same experimental configuration is used as done for the in situ experiments, (ii) the powder is free from type I stresses [31, 32], and (iii) the powder and the LMD thin-walls have the same chemical composition and heterogeneity [33]. For the 316LSS powder investigated, $a_0 = 3.5935$ Å.

The integral width of the radial peak is calculated as:

$$Integral\ width = \int I(q_r)dq_r / \max I(q_r) \tag{6}$$

The peak profiles along the azimuthal directions q_η and q_ω (see Fig. 1.b) reflect the orientation distribution within the grain and cannot be fitted with established functions defining profiles such as Pearson VII, Gaussian, Lorentzian or pseudo-Voigt distributions. Observable maxima along the profile represent individual ODs within a grain. The average position along q_η and q_ω was obtained as the intensity weighted average angle of the profile. Standard deviation of the $I_n(q_\eta)$ and $I_n(q_\omega)$ has been used to characterize the widths of the profiles.

B.3 Origin of radial peak profile asymmetry

After solidification (L_0), the radial peak profiles present an asymmetry towards lower q_r, which persists even after addition of the maximum number of layers ($L_0 + N$) independently of the investigated grain and scanning strategy. Considering that the material studied is fully austenitic, the asymmetry cannot be caused by a different phase present. Presuming a minor contribution of the large grain sizes (> 38 µm) to size broadening, the width and asymmetry indicate the presence of regions with different interplanar spacing between 400 planes. Such an asymmetry can be caused either by chemical heterogeneity [34], strain heterogeneity [19] or a combination of both.

Radial peak profile asymmetry caused by heterogeneous mechanical behavior was reported during mechanical loading for commercially pure metals (e.g., Cu [17] and Al [19]) where the effect of chemical heterogeneity on the lattice parameter can be neglected. In these studies, asymmetries observed were due to different stress states between regions with high and low dislocation densities. Observations were rationalized with a revised composite model [18]. In alloys such as 316LSS, however, inter-dendritic microsegregations are present because of a redistribution of elements having a lower solubility in the solid than in the liquid phase during solidification e.g., Cr and Mo. These microsegregations are also observed in AM 316LSS [12,35]. In DED AM process, maximum Cr and Mo microsegregations up to respectively 4 wt% and 2 wt% were reported from EDS TEM analysis in [12]. Therefore, radial peak profile asymmetry observed during experiments might also be due to microsegregations generated during solidification. The effect of the microsegregation on the change in austenite lattice parameter Δa_{fcc} at room temperature can be estimated from the chemical composition as follows [36]:

$$\Delta a_{fcc}(\text{Å}) = 0.0031\Delta w_{Mo} + 0.0006\Delta w_{Cr} + 0.00095\Delta w_{Mn} - 0.0002\Delta w_{Ni} \tag{7}$$

with the differences Δw_i in chemical composition of the elements i in weight percent (wt%) due to microsegregation of the alloying elements Mo, Cr, Mn, and Ni.

In order to estimate the change in the austenite lattice parameter Δa_{fcc}, microsegregations were quantified by line profile energy-dispersive spectroscopy using an environmental Quanta 650 FEG scanning electron microscope. An energy of 10 keV was used as it is a good compromise between the energy needed to study elements present in alloy and probed volume. Measured data were analyzed using the weighted interval rank sort method presented in [37] and used for AM 316LSS in [35]. The results confirm the trends reported in [35]. Enrichment of Mo, Cr, Mn, Ni, and Si are observed at the same locations, with maximum microsegregations level of 1.5 wt% of Mo, 2 wt% of Cr, 1 wt% of Mn, and 2 wt% of Ni. The obtained maximum segregation levels measured are in good agreement with those reported in [12] while being slightly smaller because of the probed volume due to the technique employed. Average microsegregations considering the composition difference between the first half and second half of the solid fraction measured, are ∼0.67 wt% Mo, ∼0.85 wt% Cr, ∼0.45 wt% Mn, ∼1.2 wt% Ni, and ∼0.1 wt% Si. Using Eq. 7, these microsegregations result in an austenite lattice parameter difference of $\Delta a_{fcc} = 0.00276$ Åbetween the considered segregated and non-segregated areas. Consequently, microsegregations lead to a $\Delta q_r \sim 0.0054$ Å^{-1} for the 400 scattering vector between the two different compositions.

When comparing this shift with the resolved shift $\Delta q_r \sim 0.0083$ Å^{-1} ± 0.0003 Å^{-1} between the sub-profiles used to fit the asymmetric radial profile, it shows that the shift between profiles caused by different chemical compositions corresponds to 65% of the experimentally determined value. During further addition of layers, the radial peak profile asymmetry does not evolve, while the grain-averaged residual elastic strains change significantly. The lack of change in the peak asymmetry can be rationalized considering that during AM, redistribution of segregated elements is strongly limited during fast SSTC and the microsegregation and its contribution to asymmetry is conserved. Consequently, the asymmetry observed along the radial peak profile at the initial step (L_0) and during the addition of layers ($L_0 + N$) is mainly related to chemical heterogeneity.

References

[1] K. N. Amato, S. M. Gaytan, L. E. Murr, E. Martinez, P. W. Shindo, J. Hernandez, S. Collins, and F. Medina. Microstructures and mechanical behavior of Inconel 718 fabricated by selective laser melting. Acta Materialia, 60:2229–2239, 2012.

[2] Stéphane Gorsse, Christopher Hutchinson, Mohamed Gouné, and Rajarshi Banerjee. Additive manufacturing of metals: a brief review of the characteristic microstructures and properties of steels, Ti-6Al-4V and high-entropy alloys. Science and Technology of Advanced Materials, 18:584–610, 2017.

[3] John H. Martin, Brennan D. Yahata, Jacob M. Hundley, Justin A. Mayer, Tobias A. Schaedler, and Tresa M. Pollock. 3D printing of high-strength aluminium alloys. Nature, 549:365–369, 2017.

[4] G. T. Gray, V. Livescu, P. A. Rigg, C. P. Trujillo, C. M. Cady, S. R. Chen, J. S. Carpenter, T. J. Lienert, and S. J. Fensin. Structure/property (constitutive and spallation response) of additively manufactured 316L stainless steel. Acta Materialia, 138:140–149, 2017.

[5] Y. Morris Wang, Thomas Voisin, Joseph T. McKeown, Jianchao Ye, Nicholas P. Calta, Zan Li, Zhi Zeng, Yin Zhang, Wen Chen, Tien Tran Roehling, Ryan T. Ott, Melissa K. Santala, Philip J. Depond, Manyalibo J. Matthews, Alex V. Hamza, and Ting Zhu. Additively manufactured hierarchical stainless steels with high strength and ductility. Nature Materials, 17:63–71, 2018.

[6] T. DebRoy, H. L. Wei, J. S. Zuback, T. Mukherjee, J. W. Elmer, J. O. Milewski, A. M. Beese, A. Wilson-Heid, A. De, and W. Zhang. Additive manufacturing of metallic components – Process, structure and properties. Progress in Materials Science, 92:112–224, 2018.

[7] E. Hosseini and V. A. Popovich. A review of mechanical properties of additively manufactured Inconel 718. Additive Manufacturing, 30:100877, 2019.

[8] Shunyu Liu and Yung C. Shin. Additive manufacturing of Ti6Al4V alloy: A review. Materials & Design, 164:107552, 2019.

[9] Bassem Barkia, Pascal Aubry, Paul Haghi-Ashtiani, Thierry Auger, Lionel Gosmain, Frédéric Schuster, and Hicham Maskrot. On the origin of the high tensile strength and ductility of additively manufactured 316L stainless steel: Multiscale investigation. Journal of Materials Science & Technology, 41:209–218, 2020.

[10] Thale R. Smith, Joshua D. Sugar, Chris San Marchi, and Julie M. Schoenung. Strengthening mechanisms in directed energy deposited austenitic stainless steel. Acta Materialia, 164:728–740, 2019.

[11] Andrew J Birnbaum, John C Steuben, Erin J Barrick, Athanasios P Iliopoulos, and John G Michopoulos. Intrinsic strain aging, $\sigma 3$ boundaries, and origins of cellular substructure in additively manufactured 316L. Additive Manufacturing, 29:100784, 2019.

[12] K. M. Bertsch, G. Meric de Bellefon, B. Kuehl, and D. J. Thoma. Origin of dislocation structures in an additively manufactured austenitic stainless steel 316L. Acta Materialia, 199:19–33, 2020.

[13] Kenta Yamanaka, Asumi Kuroda, Miyu Ito, Manami Mori, Huakang Bian, Takahisa Shobu, Shigeo Sato, and Akihiko Chiba. Quantifying the dislocation structures of additively manufactured Ti–6Al–4V alloys using X-ray diffraction line profile analysis. Additive Manufacturing, 37:101678, 2021.

[14] Kartik Prasad, Mitsuki Obana, Atsushi Ito, and Shiro Torizuka. Synchrotron diffraction characterization of dislocation density in additively manufactured IN 718 superalloy. Materials Characterization, 179:111379, 2021.

[15] Bo Jakobsen, Henning F. Poulsen, Ulrich Lienert, Jonathan Almer, Sarvjit D. Shastri, Henning O. Sørensen, Carsten Gundlach, and Wolfgang Pantleon. Formation and Subdivision of Deformation Structures During Plastic Deformation. Science, 312:889–892, 2006.

[16] B. Jakobsen, H. F. Poulsen, U. Lienert, X. Huang, and W. Pantleon. Investigation of the deformation structure in an aluminium magnesium alloy by high angular resolution three-dimensional X-ray diffraction. Scripta Materialia, 56:769–772, 2007.

[17] C Wejdemann, U Lienert, and W Pantleon. Reversal of asymmetry of x-ray peak profiles from individual grains during a strain path change. Scripta Materialia, 62(10):794–797, 2010.

[18] Wolfgang Pantleon, Christian Wejdemann, Bo Jakobsen, Ulrich Lienert, and Henning Friis Poulsen. Advances in characterization of deformation structures by high resolution reciprocal space mapping. In Proceedings Risø International Symposium on Materials Science, volume 31, pages 79–100, 2010.

[19] AM Diederichs, F Thiel, U Lienert, and W Pantleon. In-situ investigations of structural changes during cyclic loading of aluminium by high resolution reciprocal space mapping. International Journal of Fatigue, 117:206–216, 2018.

[20] Meriem Ben Haj Slama, Lluis Yedra, Eva Heripre, and Manas V. Upadhyay. Insight on precipitate evolution during additive manufacturing of stainless steels via in-situ heating-cooling experiments in a transmission electron microscope. Materialia, 21:101368, 2022.

[21] P Mercelis and J-P Kruth. Residual stresses in selective laser sintering and selective laser melting. Rapid prototyping journal, 2006.

[22] Hugo M Rietveld. A profile refinement method for nuclear and magnetic structures. Journal of applied Crystallography, 2(2):65–71, 1969.

[23] András Borbély. The modified Williamson-Hall plot and dislocation density evaluation from diffraction peaks. Scripta Materialia, 217:114768, 2022.

[24] D Breuer, P Klimanek, and W Pantleon. X-ray determination of dislocation density and arrangement in plastically deformed copper. Journal of applied crystallography, 33(5):1284–1294, 2000.

[25] E Macherauch, H Wohlfahrt, and U Wolfstieg. Zur zweckmäßigen definition von eigenspannungen. HTM Journal of Heat Treatment and Materials, 28(3):201–211, 1973.

[26] Manas V Upadhyay. On the thermo-mechanical theory of field dislocations in transient heterogeneous temperature fields. Journal of the Mechanics and Physics of Solids, 145:104150, 2020.

[27] Yinan Cui, Kailun Li, Chan Wang, and Wei Liu. Dislocation evolution during additive manufacturing of tungsten. Modelling and Simulation in Materials Science and Engineering, 30(2):024001, 2021.

[28] Chrysoula Ioannidou, Hans-Henrik König, Nick Semjatov, Ulf Ackelid, Peter Staron, Carolin Koerner, Peter Hedström, and Greta Lindwall. In-situ synchrotron x-ray analysis of metal additive manufacturing: Current state, opportunities and challenges. Materials & Design, 219:110790, 2022.

[29] Luis I Escano, Samuel J Clark, Andrew C Chuang, Jiandong Yuan, Qilin Guo, Minglei Qu, William Dong, Xinhang Zhang, Junye Huang, Kamel Fezzaa, et al. An electron beam melting system for in-situ synchrotron x-ray monitoring. Additive Manufacturing Letters, 3:100094, 2022.

[30] J Kieffer, V Valls, Nils Blanc, and C Hennig. New tools for calibrating diffraction setups. Journal of synchrotron radiation, 27(2):558–566, 2020.

[31] PJ Withers, M Preuss, A Steuwer, and JWL Pang. Methods for obtaining the strain-free lattice parameter when using diffraction to determine residual stress. Journal of applied crystallography, 40(5):891–904, 2007.

[32] ME Fitzpatrick and A Lodini. Analysis of residual stress by diffraction using neutron and synchrotron radiation. CRC Press, 2003.

[33] Manas Vijay Upadhyay, Meriem Ben Haj Slama, Steve Gaudez, Nikhil Mohanan, Lluis Yedra, Simon Hallais, Eva Héripré, and Alexandre Tanguy. Non-oxide precipitates in additively manufactured austenitic stainless steel. Scientific Reports, 11(1):10393, 2021.

[34] SYP Allain, S Gaudez, G Geandier, F Danoix, M Soler, and M Gouné. Carbon heterogeneities in austenite during quenching & partitioning (q&p) process revealed by in situ high energy x-ray diffraction (hexrd) experiments. Scripta Materialia, 181:108–114, 2020.

[35] S Dépinoy, M Sennour, L Ferhat, and C Colin. Experimental determination of solute redistribution behavior during solidification of additively manufactured 316l. Scripta Materialia, 194:113663, 2021.

[36] DJ Dyson. Effect of alloying additions on the lattice parameter of austenite. J. Iron Steel Inst., 208:469–474, 1970.

[37] M Ganesan, D Dye, and PD Lee. A technique for characterizing microsegregation in multicomponent alloys and its application to single-crystal superalloy castings. Metallurgical and Materials Transactions A, 36(8):2191–2204, 2005.